Mathematical modeling and Magnetic Resonance Imaging experimental study of the impregnation step: A new tool to optimize the preparation of heterogeneous catalysts

Leonor Catita, Elsa Jolimaitre, Anne-Agathe Quoineaud, Olivier Delpoux, Christophe Pichon, Jean-Marc Schweitzer

Mathematical modeling and Magnetic Resonance Imaging experimental study of the impregnation step: a new tool to optimize the preparation of heterogeneous catalysts

L. Catita[a,*], E. Jolimaitre[a] A.-A. Quoineaud[b], O. Delpoux[a], C. Pichon[a], J.-M. Schweitzer[a]

[a]*IFP Energies Nouvelles, Rond-point de l'échangeur de Solaize BP3, 69360 Solaize (France)*

[b]*Axens North America, 1800 St. James Place, Suite 500, TX 77056 Houston (United States)*

**Corresponding author: leonor.duarte-mendes-catita@ifpen.fr (Tel. +33(0) 4 37 70 32 77)*

Abstract

Optimization of supported heterogeneous catalysts requires a careful control of their synthesis conditions and in particular of the metal impregnation step. This paper presents a theoretical and experimental study of both dry and diffusional impregnation of Ni/γ-Al_2O_3 catalysts. The advanced characterization technique Magnetic Resonance Imaging was used to monitor in-situ the impregnation step, which provided the necessary information to develop the model. The model accurately describes the active phase distribution during impregnation by taking into account capillarity (in the case of dry impregnation), diffusion in the fluid phase and adsorption/desorption phenomena. It was demonstrated that the adsorption of nickel ions on the alumina surface is extremely fast, favoring the removal of metal ions from the fluid phase. As a consequence, the limiting step of impregnation is the diffusion of nickel ions in the fluid phase. A good agreement between experimental and simulated results was achieved by adjusting only two parameters, namely total concentration of the active sites and adsorption equilibrium constant. By neglecting capillary action and using the same optimized parameters, the model also allowed describing diffusional impregnation, which illustrates its robustness. This model can predict the distribution of the active phase in the support as a function of the impregnation conditions and can therefore be applied as a new tool to optimize the impregnation step of heterogeneous catalysts.

Keywords: Adsorption, Alumina, Capillarity, Catalyst, Diffusion, Impregnation, Modeling, Magnetic Resonance Imaging (MRI), Nickel, Porous media

Graphical abstract

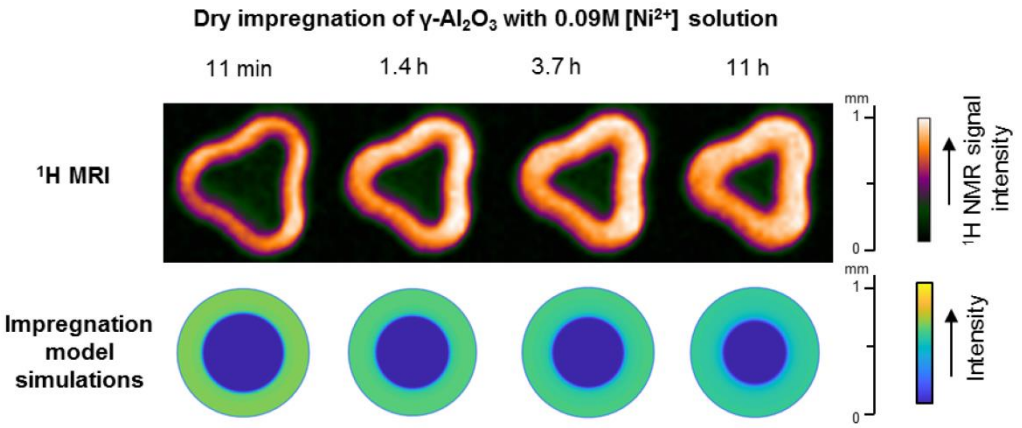

Abbreviations

EPMA: Electron Probe Micro Analysis; MRI, Magnetic Resonance Imaging; NMR, Nuclear Magnetic Resonance

Highlights

- Impregnation step of nickel supported catalysts is studied using an innovative approach combining *in-situ* characterization by Magnetic Resonance Imaging and model simulation of the impregnation step.
- The impregnation model can be applied either in the context of dry or diffusional impregnation using the same optimized parameters, which illustrates its robustness.
- This model can be used to predict the final metal distribution profile as a function of impregnation solution and support properties, which enables a better control of the impregnation step of heterogeneous catalysts.

Nomenclature

Parameter	Description	Units
*	Active site	-
C^b	Concentration of nickel in the impregnation solution	$mol.m^{-3}$
C^p	Concentration of nickel in the fluid phase inside the pore	$mol.m^{-3}$
C^*	Concentration of nickel in the adsorbed phase	$mol.kg^{-1}$
D_e	Effective diffusion coefficient	$m^2.s^{-1}$
D_m	Molecular diffusion coefficient	$m^2.s^{-1}$
D_s	Surface diffusion coefficient	$m^2.s^{-1}$
e	Average thickness	m
K_{ads}	Adsorption equilibrium constant	$m^3.mol^{-1}$
k_{ads}	Rate constant for adsorption	$m^3.mol^{-1}.s^{-1}$
k_{des}	Rate constant for desorption	s^{-1}
L	Catalyst pellet length	m
q_t	Total concentration of active sites (OH groups)	$mol.kg^{-1}$
q_*	Concentration of free active sites (OH groups)	$mol.kg^{-1}$
R	Radial coordinate	-
r_k	Net rate of adsorption reaction	$mol.kg^{-1}.s^{-1}$
R_o	Pellet radius	m
R_p	Pore radius	m
S_{BET}	Specific surface area	$m^2.g^{-1}$
TR	Repetition time	s
t_c	Contact time with the impregnation solution	s
$\bar{v}$	Penetration rate of liquid	$m.s^{-1}$
Z	Distance travelled by liquid into the pore	m

Greek letters

Parameter	Description	Units
γ	Interfacial tension	$N.m^{-1}$
ε	Porosity of the solid	-
θ	Wetting angle of the wetting fluid on the surface of the capillary	rad
μ	Dynamic viscosity	Pa.s
ρ_s	Catalyst structural density	$kg.m^{-3}$
τ	Tortuosity	-

1. Introduction

Supported metallic catalysts are widely used in heterogeneous catalysis since they provide high surface-to-volume ratio, leading to high catalytic activity at low metal loadings. During their preparation, support pellets are first impregnated with a solution containing the metal precursors of the active phase, followed by a step of ageing and thermal treatments (drying and/or calcination) [1].

Among these stages, impregnation is the key step for the genesis of the active phase. Depending on the operating conditions applied, the metal particle size, the aggregation state and the nature of the metal species in interaction with the surface can be modified [2]. A common method used at industrial scale to introduce the impregnation solution is dry impregnation, so-called incipient wetness impregnation. This method comprises filling the pore volume of the support with the corresponding volume of the precursor solution. Impregnation can also be performed in diffusional conditions, which consists in pre-filling the pore volume with water before contacting it with the impregnation solution (also called "wet" impregnation) [2,3].

In dry impregnation, metal-ions are transported into the porous support through capillarity and diffusion, while in wet/diffusional impregnation no capillary action occurs and the transport of the ions is only done by diffusion. For both methods, metal-surface interactions through electrostatic adsorption, formation of inner sphere surface complexes, surface polymerization, precipitation and dissolution of the support can take place [4]. Different parameters such as, the quantity of active sites, pore space geometry, solution pH, solution viscosity and initial metal concentration can affect the metal distribution profile at the end of impregnation.

A detailed study of the phenomena mentioned above requires the use of precise characterization techniques. In the literature, Magnetic Resonance Imaging (MRI) has been applied to monitor *in-situ* the impregnation step of supported monometallic catalysts in a non-invasive and non-destructive manner through an indirect method [5–10]. In this approach, paramagnetic and diamagnetic species, such as Ni^{2+}, Co^{2+} and Mo^{6+} are extensively used due to their influence on the ^{1}H NMR signal of water solvent as image contrast agents. Moreover, MRI yields low acquisition times (in the order of seconds to several minutes) and a spatial resolution in the order of tens of microns [11]. ^{1}H MRI images can also reflect the local concentration of the metal ion leading to

quantitative distribution profiles of metal ion inside the catalyst pellet after impregnation. Bergwerff et al. [9] provided an empirical relation between ^{1}H NMR signal intensity and Co^{2+} concentration in the impregnation solution. Based on this relation, quantitative Co^{2+} distribution plots after impregnation of a γ-Al_2O_3 were obtained. The same study was performed for the quantification of Ni^{2+} transport in γ-Al_2O_3 catalysts after impregnation [6]. Yet, none of these studies propose a theoretical impregnation model to interpret the experimental data.

Mathematical models have been reported in the literature to describe dry impregnation. Two main approaches are used to describe the capillary stage, based either on the Washburn equation or Dracy's law [12–16]. To describe the diffusion-adsorption mechanism, mass transfer in the pores is represented by Fickian diffusion, while adsorption is mainly described by the Langmuir equation or by a chemical reaction in the cases of irreversible adsorption [17–19]. Wet/diffusional impregnation is described through the diffusion-adsorption mechanism considered above [20–22]. Some of these models are coupled with experimental data. However, the active phase distribution in the catalyst is always analyzed after the solid has been subjected to a high temperature drying or calcination step, which can induce redistribution effects. Moreover, it is not possible to measure precisely the dynamics of the concentration front propagation.

Some studies were specifically dedicated to the impregnation of γ-alumina with aqueous nickel solutions. Komiyama et al. [23] described the radial concentration profiles in sphere-shaped catalysts and concluded that the initial metal concentration controlled the final distribution profile. Assaf et al. [24] proposed a mathematical model of the impregnation process of nickel-on-alumina catalysts taking into account capillarity, diffusion in the fluid phase and adsorption of nickel ions. They concluded that the concentration of the impregnation solution and the time of contact were the two main parameters that impacted the metal distribution profiles. Once again, in both examples, one cannot differentiate the thermal treatments effects from the impregnation effects as the catalysts were dried and/or calcined.

The present work focuses on nickel based catalysts supported on γ-Al_2O_3, since they are widely used in heterogeneous catalysis, particularly in hydrogenation reactions. One of the challenges during the preparation of these catalysts is to increase the metal dispersion as well as the reducibility of Ni^{2+} species in order to improve the catalytic activity. Both of these phenomena can

be controlled during the preparation process, especially during the impregnation step. Therefore, understanding the physicochemical phenomena that take place during impregnation and the critical parameters that affect this step is essential.

This study aims to determine the key parameters that control the impregnation of Ni^{2+} solution on γ-Al_2O_3 support using an innovative approach combining *in-situ* characterization and model simulation of the impregnation step. Hence, ^{1}H MRI is applied to follow *in-situ* the transport dynamics of the metal precursor inside the support during two different impregnation protocols : dry and diffusional impregnation. Based on the experimental results, a mathematical model that can be used either in the context of dry or diffusional impregnation is proposed. The impregnation model takes into account the transport of nickel ions by capillary forces (in the case of dry impregnation), diffusion into the support pores and adsorption/desorption on the active sites of the support.

2. Materials and Methods

2.1. Impregnation method

A pre-shaped γ-Al_2O_3 support in the form of trilobal extrudate, prepared by kneading-extrusion of boehmite powder, with 1.2-1.3 mm diameter and 3-6 mm of length was chosen as support. Mercury porosimetry and nitrogen adsorption-desorption methods were applied for textural characterization. This support is characterized by a total porous volume of 0.6 cm^3/g and a specific surface S_{BET} of 250 m^2/g. The tortuosity (τ) of the support (equal to 2.5) was determined by ^{1}H PFG-NMR technique applied to toluene inside the porosity of the support as described in [25]. The point of zero charge (PZC) is 8-8.5.

Nickel nitrate ($Ni(NO_3)_2.6H_2O$) of 98.5% purity (Sigma-Aldrich, CAS number 13478-00-7) was used as the metal precursor. Impregnation solutions were prepared by dissolving the desired quantity of the metal precursor in a certain volume of deionized water. The concentration of nickel in the impregnation solution ranged from 0.05 to 0.2 M, which corresponds to a %wt of metal from 0.25 (0.10 Ni atoms/nm^2) up to 0.95 (0.39 Ni atoms/nm^2) in the final nickel-based catalysts. The pH of the solutions varied from 5 to 6.

The first impregnation method called “dry” impregnation was carried out by contacting a non-wetted alumina extrudate with the impregnation solution containing the active element for 30s, the excess solution being removed by wiping as reported in [10]. Right after impregnation, the catalyst pellet was introduced in a capillary tube with 1.7 mm diameter and then in a 5 mm NMR tube, as described in Figure 1. The capillary tube ensured that the sample was vertically positioned and parallel to the z direction of the main magnetic field and the z gradient of imaging. The diffusion process continued inside the NMR tube. This method allows one to be as close as possible to the traditional incipient wetness impregnation protocol, even if the volume of impregnation solution used here does not exactly correspond to the pore volume of the support. Yet, both protocols consist in contacting a non-wetted pellet with an ionic aqueous solution, which implies a first step governed by capillary forces. Therefore, the physico-chemical phenomena that take place are the same.

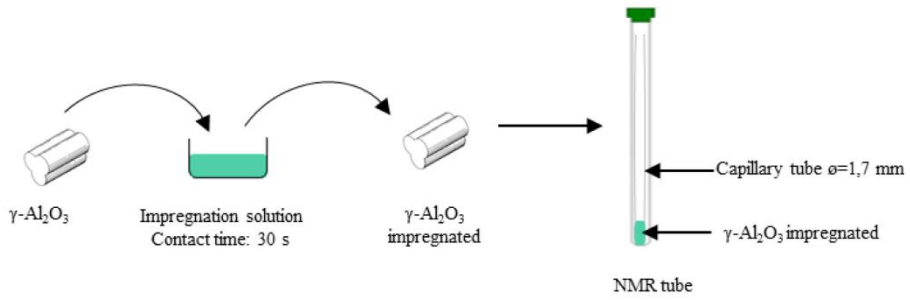

Figure 1 – Protocol of “dry” impregnation using a non-wetted support (closest of the traditional incipient wetness impregnation)

In the second impregnation method used is this work called “diffusional” impregnation, the alumina extrudate was first saturated with water (same solvent as the impregnation solution) and then contacted with the impregnation solution according to the method described above, as represented in Figure 2.

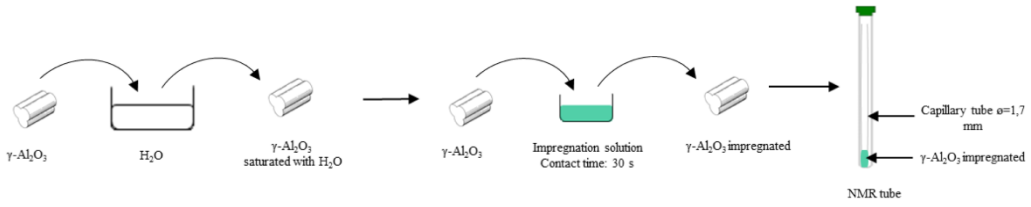

Figure 2 – Protocol of “diffusional” impregnation using a pre-wetted support

2.2. Magnetic Resonance Imaging experiments

The transport of nickel ions inside γ-alumina was monitored through an indirect approach by measuring the ^{1}H MRI signal of water inside the porosity of the support. The paramagnetic effect of the metal on the ^{1}H MRI signal induces contrast in MRI images, which allows visualizing its distribution on the porous support.

MRI experiments were performed in a Bruker Avance 400MHz (^{1}H) spectrometer. The spectrometer was equipped with a 5mm imaging probe (Micro5) and xyz gradient amplifiers (300×300×300 G/cm) at 60A current, which allowed selecting the voxels of interest. Experiments were carried out at a temperature of 17°C.

Axial-oriented ^{1}H MRI images were obtained using a Single Point Imaging (SPI) sequence [26] with a field of view (FOV) of 3×3×1 mm and 64×64×8 acquisition points, resulting in a voxel size of 47 µm× 47 µm×125 µm. A slice thickness of 1 mm was defined. For each MRI experiment, 8 images were obtained, each one corresponding to a certain position along the z axis of the pellet. An excitation pulse of 90° and 22.5 µs was set. The encoding time was defined to 200 µs, while the repetition time (TR) was varied from 10 to 20 ms in order to adapt the total scan time to the transport rate of nickel ions during impregnation. This resulted in a total scan time between 5 to 11 minutes. Due to the imposed value of the repetition time, which is lower than T_1 relaxation time of water protons near nickel ions, images were T_1-weigthed. T_1 values were determined using a RAREVTR (Rapid Acquisition with Relaxation Enhancement with variable repetition time TR) sequence [27]. Proton T_1 of pure water inside γ-alumina system was 370 ms, while this value was decreased to approximately 15ms in the presence of nickel ions at the lowest concentration used. Paravision 5.1 software was used for MRI images acquisition.

2.3. Electron Probe Microanalysis measurements

Electron Probe Microanalysis (EPMA) measurements allows one to localize and to carry out a semi-quantification of the elements. Before EPMA measurements, catalysts were calcined at 450°C for 2h. For EPMA analysis, catalysts were embedded in a prepolymerized epoxy resin and polished to their diameter. A carbon coating was deposited at the surface of each sample. Analyses were performed on a JEOL JXA 8100 electron microprobe at 20 kV and 200 nA. Nickel was

quantified using the Kα lines, with a detection limit of 160 ppm. The average distribution profile along the cross section was recorded by measuring between three to five different profiles along different 3-fold symmetry axes of the pellets. The analysis step was approximately 50 µm, excluding the cases where the metal was in an egg-shell profile, for which an analysis step of 10 µm in each side of the crust was set.

2.3. Mathematical modeling of the impregnation step

The impregnation model developed in this work takes into account the following phenomena: capillarity, diffusion in the fluid phase, surface diffusion and surface interaction (adsorption/desorption).

Figure 3 describes the different phenomena involved in both impregnation methods. In the case of non-wetted support (dry impregnation protocol), during the contact time between the solution and the pellet, the impregnation solution penetrates into the porous support by the action of capillary forces. Simultaneously to this convective flow, diffusion of nickel ions in the fluid and in the adsorbed phase (surface diffusion) as well as adsorption/desorption of the solute by the pore walls also occur. Once the support is removed from the solution, one can consider that the catalyst particle is completely wetted. From this step, the transport of solute into the support pores is only done by diffusion (in the fluid and adsorbed phase), while adsorption of the solute occurs simultaneously. This stage is called the diffusion-adsorption stage.

In the context of diffusional impregnation, no capillary action takes place, since the support was pre-saturated with water before impregnation. Therefore, only the diffusion-adsorption stage is considered.

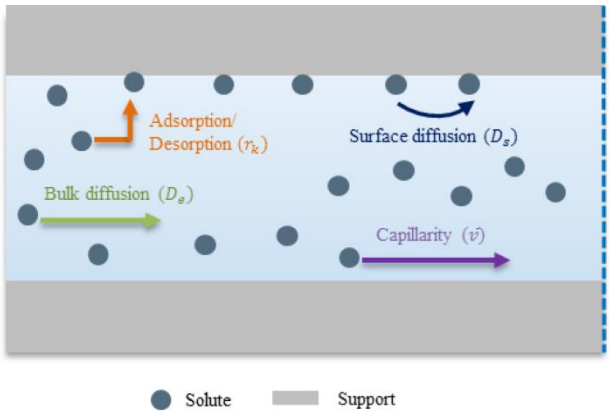

Figure 3 – Physicochemical phenomena involved in the impregnation (capillarity only for dry impregnation) (adapted from [3])

The mathematical model was developed based on the following assumptions:

a) Due to the difficulty to solve the equations for a trilobic shape, a cylindrical particle with an equivalent diameter defined as follows $D_{eq} = \frac{4.V}{S}$ (i.e., same volume over external surface ratio) was assumed [28];

b) The impregnation solution is considered as an incompressible and Newtonian fluid;

c) Properties of the impregnation solution (surface tension, wetting angle and viscosity) are the same as those of water, since nickel diluted solutions were used;

d) Flow of the impregnation solution in the pore is laminar and therefore, the velocity profile can be characterized by Poiseuille's law;

e) The gravity force is negligible compared to capillary and friction forces; also the impact of air bubbles on the penetration of water for dry impregnation was neglected [29,30];

f) Only radial concentration gradients inside the pellet are considered (no axial concentration gradients);

g) Diffusive mass transfer inside the particles is represented by Fickian diffusion, with an effective diffusion coefficient D_e in the fluid phase and a surface diffusion coefficient D_s in the adsorbed phase. In order to take into account the effect of the porous network in the the molecular diffusion regime, the effective diffusion coefficient D_e is corrected by two textural parameters: the porosity ε of the solid and the tortuosity τ as follows :

$$D_e = \frac{D_m \varepsilon}{\tau} \qquad \textbf{(Eq. 1)}$$

Where D_m corresponds to the molecular diffusion coefficient of nickel ions ;

h) According to the acidic pH of impregnation solution, only one type of nickel species is presented, namely nickel ions in the form of hexa-aqua complex, $[Ni(H_2O)_6]^{2+}$ [31];

i) Adsorption of the nickel ions is represented by a first order reversible reaction involving two OH surface sites [32] (see (Eq. 2)):

$$Ni + 2 * \underset{k_{des}}{\overset{k_{ads}}{\rightleftarrows}} Ni *_2 \qquad \textbf{(Eq. 2)}$$

Where $*$ represents the active site (OH group), $Ni *$ corresponds to Ni chemisorbed on two surface sites and k_{ads} and k_{des} refer to the rate constants for adsorption and desorption, respectively.

j) The total concentration of adsorption sites is q_t;

k) All surface sites have the same energetics for adsorption;

l) There is no interaction between adsorbed molecules.

Thus, the mass balance of nickel ions in the fluid phase along the crossed section area of a cylindrical catalyst particle, having a R_o radius, yields the following equation [33,34]:

$$\varepsilon \cdot \frac{\partial C^p}{\partial t} = \frac{D_e}{r} \cdot \frac{\partial}{\partial r}\left(r \cdot \frac{\partial C^p}{\partial r}\right) + \frac{\varepsilon}{r \cdot \tau} \cdot \frac{\partial}{\partial r}(r \cdot \bar{v} \cdot C^p) + r_k . \rho_s . (1 - \varepsilon) \qquad \textbf{(Eq. 3)}$$

Where,

$\varepsilon \cdot \frac{\partial C^p}{\partial t}$ corresponds to the accumulation term, in which ε is the porosity, C^p is the concentration of nickel ions in the fluid phase inside the pore and t is time;

$\frac{D_e}{r} \cdot \frac{\partial}{\partial r}\left(r \cdot \frac{\partial C^p}{\partial r}\right)$ corresponds to the diffusive term, in which D_e is the effective diffusion coefficient;

$\frac{\varepsilon}{r.\tau} \cdot \frac{\partial}{\partial r}(r \cdot \bar{v} \cdot C^p)$ corresponds to the convective flow, in which τ is the tortuosity of the solid and $\bar{v}$ is the penetration rate of the liquid that is obtained through the Washburn model [35]; this term is neglected in the case of diffusional impregnation ($\bar{v} = 0$). From the Washburn model one can obtain the distance $z(t)$ that the impregnation solution reaches into the pore as a function of time. A detailed description of how z(t) is calculated, is given in Supplementary Data (Appendix A). Assuming that at $t = 0,\ z = 0$, one gets:

$$z = \sqrt{\frac{R_p \cdot \gamma \cdot cos\theta}{2 \cdot \mu} \cdot t} \qquad \textbf{(Eq. 4)}$$

with R_p the pore radius, γ the surface tension, θ the wetting angle and μ the viscosity of the impregnation solution.

In (Eq. 3), $r_k . \rho_s . (1 - \varepsilon)$ corresponds to the kinetic term, where the net rate of adsorption r_k is given by [33]:

$$r_k = k_{ads} C^p \, {q_*}^2 - k_{des} C^* \qquad \textbf{(Eq. 5)}$$

where, C^* is the concentration of nickel in the adsorbed phase.

At equilibrium, the net rate of adsorption is zero ($r_k = 0$). Therefore, the adsorption equilibrium constant K_{ads} is given by:

$$K_{ads} = \frac{k_{ads}}{k_{des}} = \frac{C^*}{C^p {q_*}^2} = \frac{C^*}{C^p (q_t - 2C^*)^2} \qquad \textbf{(Eq. 6)}$$

Note that (Eq. 6) cannot be expressed in the form of the Langmuir adsorption isotherm since two surface sites are involved during adsorption.

For the mass balance in the adsorbed phase (see (Eq. 7) [34]), the effective diffusion coefficient D_e is replaced by the surface diffusion coefficient (D_s).

$$\frac{\partial C^*}{\partial t} = \frac{D_s}{R_o} \cdot \frac{\partial}{\partial r}\left(r \cdot \frac{\partial C^*}{\partial r}\right) + r_k \qquad \textbf{(Eq. 7)}$$

The boundary conditions at the center of the pellet are:

$$\left.\frac{\partial C^p}{\partial r}\right|_{r=0} = 0, \forall \, t$$

$$\left.\frac{\partial C^*}{\partial r}\right|_{r=0} = 0, \forall \, t$$

At the surface of the pellet (i.e, outside of the pores), the boundary conditions depend on the impregnation stage:

- First stage (contact with the impregnation solution): $C^p|_{r=R_o} = C^b, \forall\, t$, where C^b is the concentration of nickel in the impregnation solution.
- Second stage (after retrieving the pellet from the impregnation solution):

$$C^p|_{r=R_o} = 0, \forall t$$

$$\left.\frac{\partial C^p}{\partial r}\right|_{r=R_o} = 0, \forall t$$

The initial conditions for the first stage (contact with the impregnation solution) are:

$$t = 0: \begin{cases} z = 0 \\ C^* = 0, \forall\, r \\ C^p = 0, \forall\, r \end{cases}$$

The initial conditions for the second stage ($t > t_c$, where t_c is the contact time with the impregnation solution) are simply the state of the system at the end of the first stage.

Material balances were solved using a cylindrical discretization meshing. The size of the equivalent cylindrical particle depends on the equivalent diameter that respects the volume-to-surface (V/S) ratio. Simulations were made for each time step needed to acquire an MRI image.

3. Results

3.1. MRI experimental measurements

Figure 4 shows the ^{1}H MRI images recorded on γ-alumina pellets at several points in time after dry impregnation with various nickel concentrations. These images show T_1 contrast, which exhibits the water ^{1}H signal influenced by Ni^{2+} ions in the neighborhood of water molecules. As a consequence, the dark area corresponds to a low concentration of metal ion (T_1 longer - weak ^{1}H signal intensity), while the bright area (shown in orange) corresponds to a higher concentration of these ions (T_1 shorter - strong ^{1}H signal intensity). Initially, nickel ions are only observed close to the edges of the pellet. As time elapses, an evolution of the bright area is observed, which corresponds to a progression of Ni^{2+} ions inside γ-alumina. In these examples, a non-uniform ^{1}H MRI signal is observed in the entire pellet even after several hours of impregnation with 0.05M [Ni^{2+}] solution, which is interpreted as an egg-shell distribution of nickel ions. On the contrary, for a 0.2M [Ni^{2+}] solution, a homogeneous metal profile is observed.

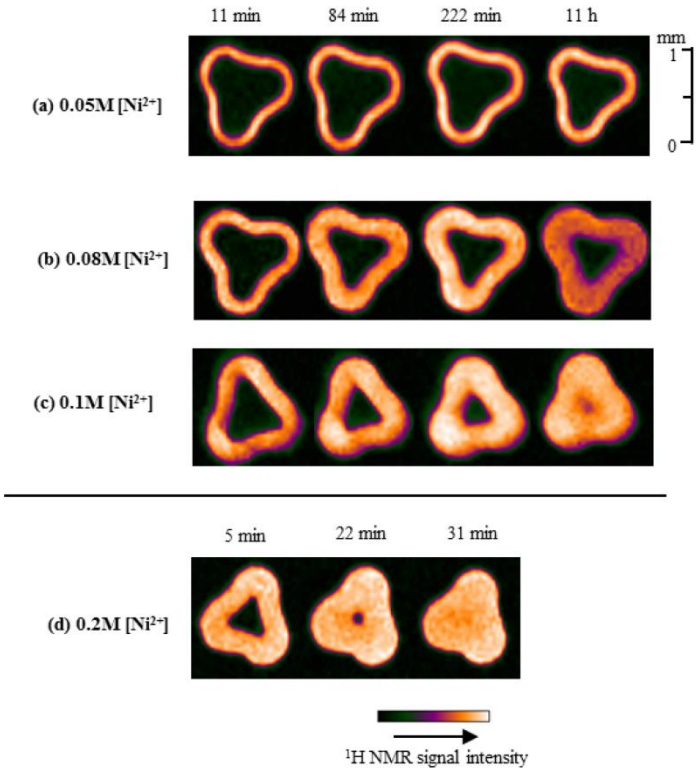

Figure 4 – ^{1}H MRI images recorded on γ-alumina pellets at several points in time after dry impregnation with (a) 0.05M [Ni^{2+}] (b) 0.08M [Ni^{2+}] (c) 0.1M [Ni^{2+}] and (d) 0.2M [Ni^{2+}] solutions. These images correspond to the center of the pellet.

As expected, the transport of Ni^{2+} ions is favored by high metal concentrations in impregnation solution. These MRI experiments suggest that: in a first stage, the water solvent is transported together with the metal ions into the empty pores by capillary flow and diffusion. This observation is in agreement with the study of Espinosa et al. [6]. Second, surface interaction is not negligible as it seems to hamper the transport of the metal ions through the porous support. Such interaction can be a result of an adsorption reaction through the formation of covalent bonds.

^{1}H MRI images were also acquired at different extrudate lengths along the z-axis as illustrated in Figure 5. In order to avoid the influence of "edge effects" of the pellet on the MRI image, these slices were obtained close to the pellet center, which explains the similarity of the images. One can observe that close to the pellet center, the axial concentration profiles remain constant regardless the position in the z axis, proving the assumption that the transport of nickel ions mainly takes place in the radial direction.

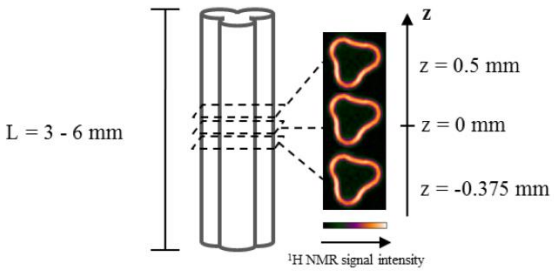

Figure 5 - ^{1}H MRI images corresponding to transport of 0.05 M [Ni^{2+}] solution within the porosity of a γ-Al_2O_3 pellet at different positions along the z axis (z=0 corresponds to the pellet center) after 11 minutes of dry impregnation (L corresponds to the pellet length)

Additionally, for dry impregnation experiments, the radial intensity profiles of the MRI images were compared with the average concentration profiles obtained by EPMA (see Supplementary Data – Appendix B). Both techniques show the presence of nickel ions in the same positions of the catalyst pellet regarding the spatial resolution of each technique.

Impregnation was also carried out with pre-wetted supports. Figure 6 shows ^{1}H MRI images obtained from a pre-wetted extrudate after impregnation with 0.1M [Ni^{2+}] solution at several points in time. The results show that in diffusional conditions the transport of nickel ions into the porosity is much slower than in dry conditions (see Figure 4 (c)).

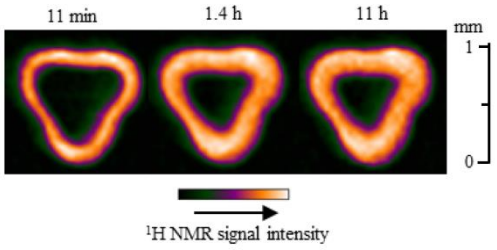

Figure 6 - ^{1}H MRI images recorded on γ-alumina pellet at several points in time after diffusional impregnation with 0.1M [Ni^{2+}] solution. These images correspond to the center of the pellet.

3.2. Model implementation

3.2.1. Evaluation of the mass transfer limiting steps

The textural properties of the support, the fluid phase properties and the molecular diffusion of nickel ions in water were evaluated using classical characterization techniques or extracted from literature. Their values are reported in Table 1.

Table 1 – Characteristic parameters for simulation of impregnation profiles

Parameter	Value
Pellet radius, $\boldsymbol{R_o}$ (m)	0.00056
Pellet length, $\boldsymbol{L}$ (m)	0.0045
Pore radius, $\boldsymbol{R_p}$ (m)	4.7×10^{-9}
Porosity, $\boldsymbol{\varepsilon}$	0.65
Structural density, $\boldsymbol{\rho_s}$ (kg/m^3)	3600
Tortuosity, $\boldsymbol{\tau}$	2.5
Surface tension, $\boldsymbol{\gamma}$ (N.m)	72×10^{-2} [36]
Viscosity, μ (Pa.s)	1×10^{-3} [36]
Wetting angle, $\boldsymbol{\theta}$ (rad)	1.05 [36]
Molecular diffusion coefficient of nickel ions, $\boldsymbol{D_m}$ (m^2/s)	7.05×10^{-10} (at 25°C) [37]

Regarding (Eq. 3), (Eq. 6) and (Eq. 7), four other parameters required for simulation of impregnation profiles are still unknown: rate constant for adsorption k_{ads}, surface diffusion coefficient D_s, adsorption equilibrium constant K_{ads} and total concentration of the active sites q_t.

(Eq. 4) was used to predict the advancing front of water during the capillary stage. Figure C.1 in Supplementary Data indicates that after only 4 seconds of impregnation, water is already present in the entire porosity, showing that capillarity is nearly an instantaneous phenomenon. Even so, experimental results reported in Figure 4 show an egg-shell profile of nickel ions after several minutes of impregnation. The fact that nickel ions are not transported together with the capillary flow of water can be explained by an extremely fast adsorption reaction. For this reason, the rate constant for adsorption k_{ads} can be considered as non-limiting and therefore a very high value of 1 m^3/(kg.s) was assumed.

Based on these results, impregnation seems to be limited either by surface diffusion of nickel in the adsorbed phase or diffusion of nickel ions in the fluid phase.

In order to investigate in more detail the presence of a surface diffusion mechanism, simulations were carried out to obtain the concentration profiles in the adsorbed and fluid phases with and without surface diffusion. Figure 7 and Figure 8 report the model predictions for nickel concentration profiles after 11h of dry impregnation with a 0.05M [Ni^{2+}] solution. For these simulations, surface diffusion coefficient (D_s) was considered equal to $10^{-12}\ m^2/s$, while random (not optimized) values of adsorption equilibrium constant K_{ads} and total concentration of the active sites q_t were used. Regardless the values of (q_t, K_{ads}), one can observe that in the presence of surface diffusion, nickel concentration profiles in the adsorbed and fluid phase are broadened, while in the absence of this mechanism, sharp profiles are obtained. These results emphasize the totally different behavior of the system depending on the limiting mass transfer mechanism:

- When surface diffusion is very slow, the dynamics of the system is solely controlled by fluid phase diffusion. However, the effective fluid phase diffusion coefficient is impacted by adsorption: molecules that diffuse towards the center of the pellet are immediately adsorbed on the surface, which slows down the advance of the concentration front. Hence, the effective diffusivity is much smaller than the molecular diffusivity. The same effect can be encountered for the diffusion in macro/mesopores surrounding nanocrystals of zeolites [38].
- If surface diffusion is non-negligible, then both the adsorbed and the fluid phase follow the normal trend for diffusion phenomena: the molecules in both phases diffuse until the concentration gradients (i.e. the driving force for diffusion) get negligible, that is, until the concentration is homogeneous at any position in the pellet. Yet, it should be mentioned that the adsorption equilibrium constant could slow down the advance of the concentration front in both cases.

Consequently, the experimental results in Figure 4 (a), which depicts a “frozen” stiff concentration front located in a thin layer at the support surface are not compatible with a surface diffusion mechanism.

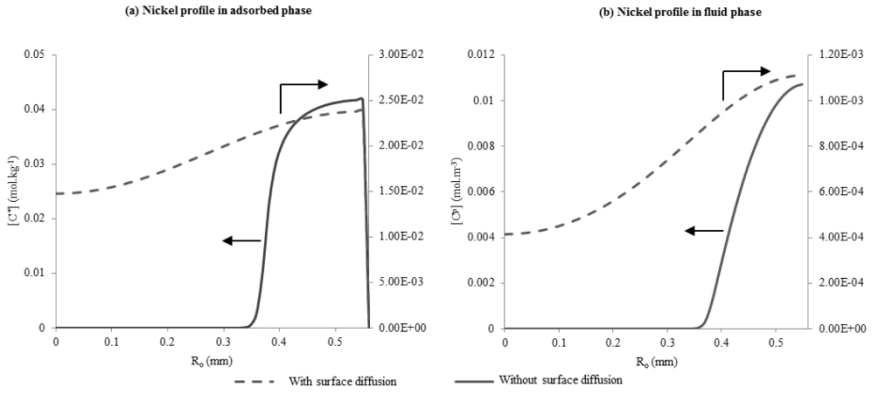

Figure 7 - Model simulations for nickel concentration profiles after 11h of dry impregnation using 0.05M [Ni^{2+}] solution: metal concentration profiles in the (a) adsorbed and (b) fluid phase as a function of the pellet radius with and without surface diffusion $(\boldsymbol{q_t}, \boldsymbol{K_{ads}})$=(0.11, 5500)

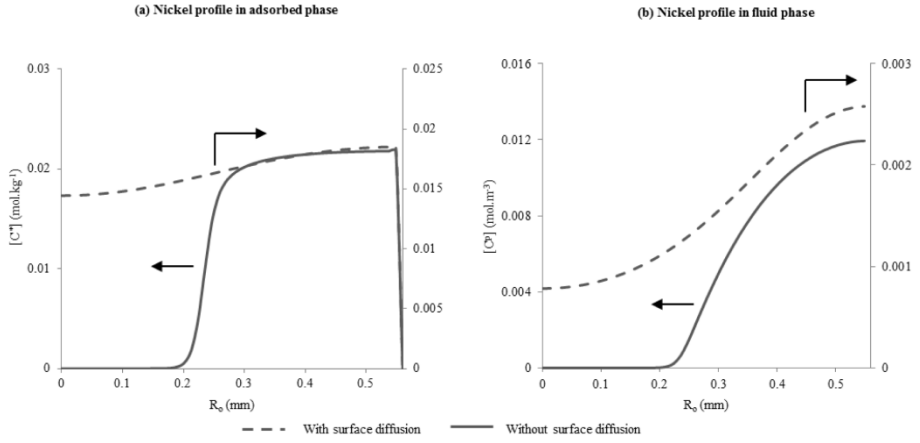

Figure 8 - Model simulations for nickel concentration profiles after 11h of dry impregnation using 0.05M [Ni^{2+}] solution: metal concentration profiles in the (a) adsorbed and (b) fluid phase as a function of the pellet radius with and without surface diffusion $(\boldsymbol{q_t}, \boldsymbol{K_{ads}})$=(0.05, 41833)

Therefore, the controlling mechanism of impregnation process is the diffusion of nickel ions in the fluid phase. The effective diffusivity (D_e) depends on the molecular diffusion of nickel ions (D_m), tortuosity (τ) and the concentration of metal ions in the fluid phase (C^p). The latter is strongly affected by the total concentration of the active sites (q_t) and the adsorption equilibrium constant (K_{ads}). Among these parameters, only q_t and K_{ads} were unknown. These parameters were estimated from the comparison of experimental nickel distribution profiles observed in MRI images with those obtained from the impregnation model as explained in the following section.

Additionally, as can be seen in Figure 7 and Figure 8, the concentration profiles in the adsorbed and fluid phase are similar. As a result, for the following simulations only the global position of the front will be shown.

3.2.2. Parameter estimation

q_t and K_{ads} were obtained by optimizing the best fitting of experimental and simulation results of the average thickness profile (e) ensuring a normal distribution of residuals with minimization of the objective function presented in (Eq. 8):

$$\sum \left(e_{simulation} - e_{experimental}\right)^2 \quad \textbf{(Eq. 8)}$$

Five experiments for both dry and diffusional impregnation were used for parameter estimation and two experiments were used for parameter validation.

The optimal values of q_t and K_{ads} were estimated based on a three steps optimization procedure. The variation range (minimal and maximal values) were fixed using preliminary simulations. First, a latin hypercube simulation design was implemented, in order to explore the input parameter space and evaluate the sensitivity of the objective function with respect to the two parameters. Then, a response surface of the objective function was built from the simulation results obtained on the design, and finally an optimization procedure was performed on this response surface in order to obtain the optimal parameter values that minimize the objective function (see Table 2). This procedure allows one to save computational time by reducing the number of simulations: the optimization procedure is very fast due to the use of the response surface in replacement of the simulator. All this procedure was implemented using an IFPEN in-house optimization tool [39].

Table 2 – Design plan of simulation and optimization results

Latin hypercube design simulations		
q_t **(mol.kg^{-1})**	K_{ads} **(m^3.mol^{-1})**	$\sum(e_{simulation} - e_{experimental})^2$
0.05	41833	0.93
0.075	1000	0.47
0.0856	25914	0.09
0.1	25500	0.07
0.125	50000	0.12
0.15	9167	0.34
0.175	33667	0.57
0.2	17333	0.73
Optimal parameters from surface response modeling		
q_t **(mol.kg^{-1})**	K_{ads} **(m^3.mol^{-1})**	$\sum(e_{simulation} - e_{experimental})^2$
0.11	5500	0.06

Figure 9 shows the model predictions (using optimal parameters) for nickel distribution profiles at several points after dry impregnation for various nickel concentrations, whereas Figure 10 illustrates model simulations for diffusional impregnation.

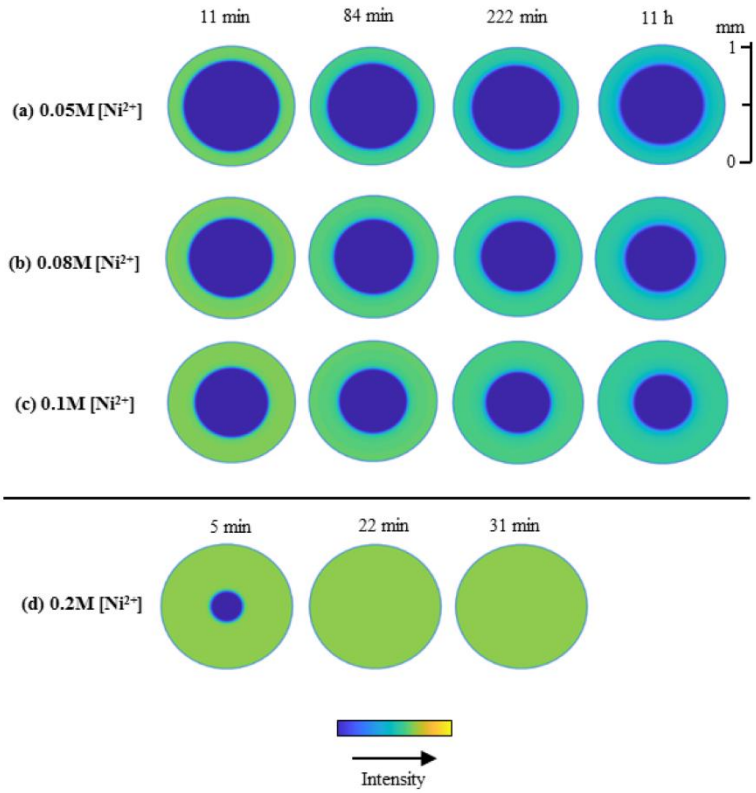

Figure 9 – Model predictions using optimal parameters for nickel distribution profiles at several points in time after dry impregnation for various nickel concentrations.

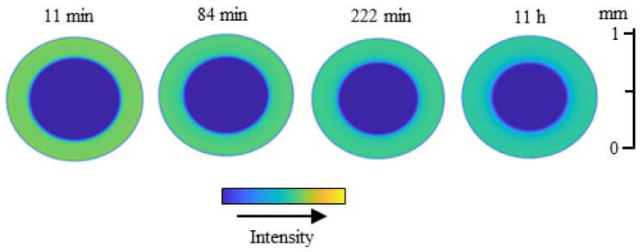

Figure 10 - Model predictions using optimal parameters for nickel distribution profiles at several points in time after diffusional impregnation for 0.1M [Ni^{2+}].

Figure 11 shows the comparison between simulated data (continuous line) and experimental results (points) obtained by MRI, for the average thickness profile of nickel ions along the radial distance in the pellet. The tendencies are globally respected: the higher the concentration, the faster the nickel concentration front penetrates into the extrudate. Also, the model predicts well the slower kinetic for diffusional impregnation compared to dry impregnation (respectively the purple and orange curves). However, some discrepancies can be seen, particularly for intermediate

concentrations. This can be probably be explained for instance by an over simplification of the adsorption equilibrium constant, as discussed further on.

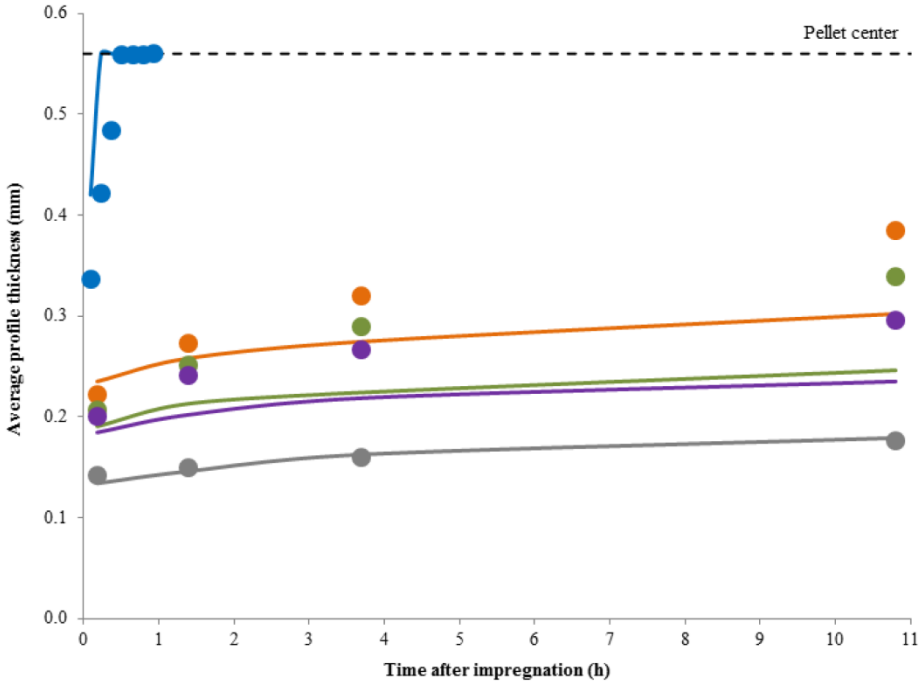

Figure 11 – Comparison between experimental and simulated data using optimal parameters (q_t, K_{ads}) = (0.11, 5500) in case of (a) dry impregnation for different nickel concentrations: 0.05M [Ni^{2+}] (in grey), 0.08M [Ni^{2+}] (in green), 0.1M [Ni^{2+}] (in orange), 0.2M [Ni^{2+}] (in blue) and (b) diffusional impregnation with 0.1M [Ni^{2+}] (in purple)

Table 3 summarizes the parameters obtained through model simulations.

Table 3 – Model parameters

Parameter	Value
k_{ads} (m^3/(kg.s))	1
D_s (m^2/s)	0
q_t (mol/kg)	0.11
K_{ads} (m^3/mol)	5500

3.3. Validation of the impregnation model

The parameters reported in Table 1 and Table 3 were used to validate the impregnation model. Figure 12 and Figure 13 illustrate the ^1H MRI images recorded on γ-Al_2O_3 extrudates at several

points in time after dry impregnation with 0.07M [Ni^{2+}] solution and after diffusional impregnation using 0.2M [Ni^{2+}] solution together with the corresponding model simulations. The evolution of nickel distribution profiles show the same trend both in experimental and simulated results. For both examples, non-uniform profiles were obtained, which is evidenced by a higher intensity near the edges, corresponding to the presence of nickel ions and a low signal near the core of the pellet (absence of nickel ions).

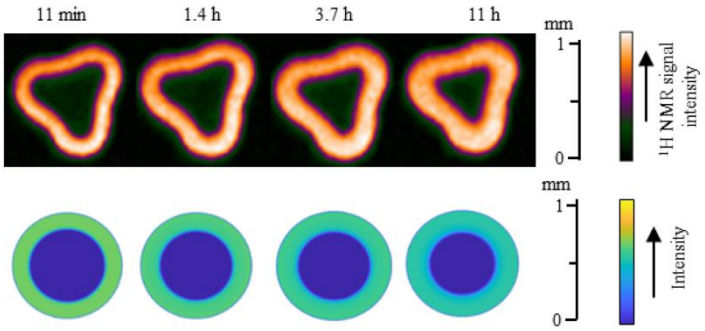

Figure 12 – ^{1}H MRI images at the center of the pellet (top) and model simulations (bottom) recorded on γ-Al_2O_3 support at several points in time after dry impregnation with 0.07M [Ni^{2+}] solution

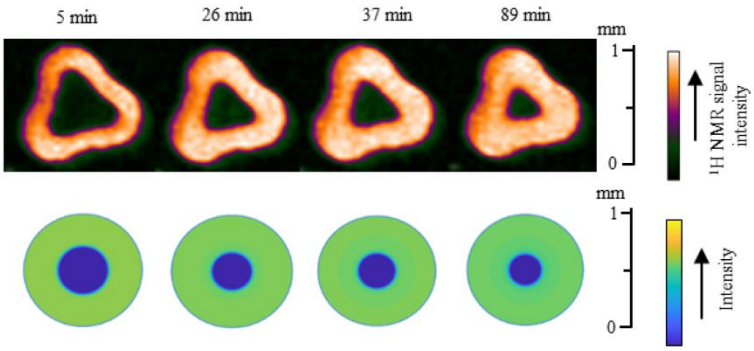

Figure 13 - ^{1}H MRI images at the center of the pellet (top) and model simulations (bottom) recorded on γ-Al_2O_3 support at several points in time after diffusional impregnation with 0.2M [Ni^{2+}] solution

It should be noted that the same parameters predict the metal distribution profile for both dry and diffusional impregnation, which illustrates the robustness of the model.

3.4. Model parametric sensitivity

The impact of the two parameters q_t and K_{ads} on the objective function (Eq. 8) is depicted in Figure D.1 in Supplementary Data. Whereas the objective function displays a clear minimum for

parameter q_t, it is not the case for the adsorption equilibrium parameter K_{ads}. Therefore, the parameters q_t and K_{ads} were varied of respectively 10% and 50% in order to analyze their influence on the nickel distribution profiles. Figure 14 and Figure 15 show the results of these simulations for the case of dry impregnation with a 0.05M [Ni^{2+}] solution.

According to Figure 14, a variation of only 10% of q_t (represented in orange) significantly impacts the nickel distribution profile. By decreasing q_t, the average profile thickness of the advancing front of nickel ions increases. Indeed, for low values of q_t, more nickel ions remain in the fluid phase, which favors their transport inside the pellet. On the contrary, the variation of K_{ads} has only a very small impact on the distribution profiles (see Figure 15).

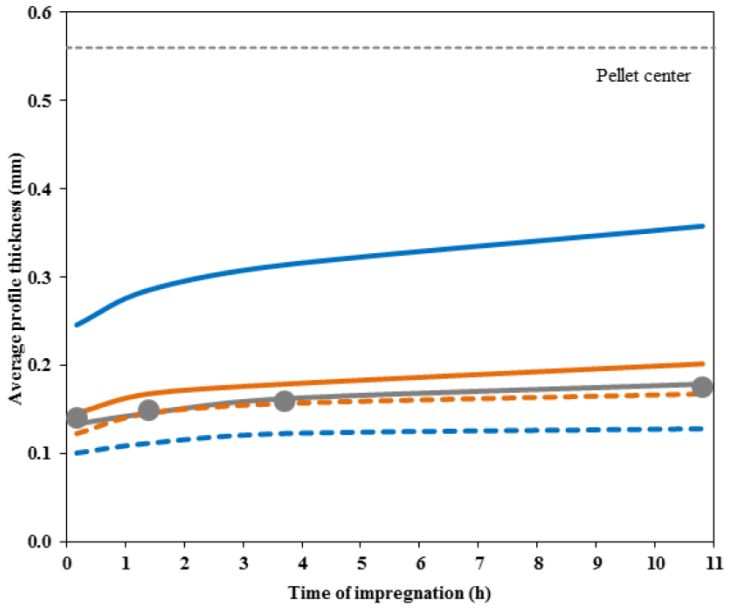

Figure 14 – Simulations of nickel distribution profiles for dry impregnation with 0.05M [Ni^{2+}] obtained by varying the optimal $\boldsymbol{q_t}$ (represented in grey) in $\pm$ 10% (represented in orange : solid line corresponds to -10% and the dashed line to +10%) and in $\pm$ 50% (represented in blue: solid line corresponds to -50% and the dashed line to +50%). The points in grey correspond to the experimental data. For these simulations $\boldsymbol{K_{ads}}$ = 5500 $m^3.mol^{-1}$.

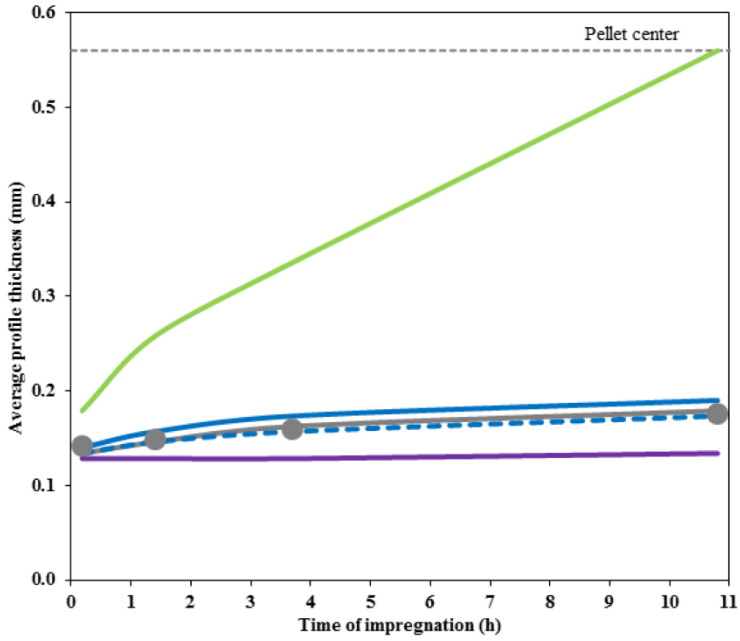

Figure 15 - Simulations of nickel distribution profiles for dry impregnation with 0.05M [Ni^{2+}] obtained by varying the optimal $\boldsymbol{K_{ads}}$ (represented in grey) in $\pm$ 50% (represented in blue: solid line corresponds to -50% and the dashed line to +50%). Simulations for irreversible adsorption (in purple) and neglecting adsorption (in green) are also shown. The points correspond to the experimental data. For these simulations $\boldsymbol{q_t}$ = 0.11 $mol.kg^{-1}$. Simulations by varying the $\boldsymbol{K_{ads}}$ in $\pm$ 10% are not shown here: no influence was observed in this range of variation.

Still, one can see in Figure 15 that for irreversible adsorption (represented in purple), the model predicts no evolution of the concentration front with time, in contradiction with experimental observations. And, as expected, neglecting adsorption (represented in green) induces a too much faster progress of the concentration front towards the pellet center. Hence, even though the value of K_{ads} cannot be accurately evaluated from these experiments, it is clear that the adsorption isotherm is highly favorable but not irreversible.

4. Discussion

Overall, a satisfactory agreement between experimental and simulated data is achieved, meaning that most of the hypotheses adopted in the model are verified within the experimental conditions studied. The proposed model demonstrates that the limiting impregnation step is the effective diffusion of nickel ions in the fluid phase, which is strongly impacted by the adsorption of nickel ions on the surface. As also observed experimentally, the model demonstrates that by increasing

the metal concentration in the pores, nickel ions migrate deeper within the pellet, eventually reaching the pellet center. The metal concentration can be increased by preparing a more concentrated impregnation solution or by choosing the dry impregnation mode. Indeed, capillary forces push a large amount of nickel forward during the first seconds after contacting the non-wetted pellet with the aqueous solution. Thus, the initial nickel concentration in the pores provides the necessary driving force to overcome the competition between adsorption and bulk diffusion.

The differences observed between the average thickness profile of nickel ions obtained from simulated and experimental data in Figure 11 can be attributed to several simplifying assumptions adopted for the mathematical modeling of the impregnation step. These can be firstly attributed to the simplification of a cylindrical geometry instead of a trilobic geometry of the catalyst.

Secondly, the quadratic form of the kinetic term in (Eq. 5), which is a direct consequence of the assumption that one nickel ion Ni^{2+} occupies two OH^- sites (see (Eq. 2)) on the alumina surface, induces an "non-classical" adsorption isotherm shape, i.e. different from the well-known isotherms such as Langmuir or Freundlich. Moreover, this assumption does not take into account the constrain that the two OH^- groups have to be located in close proximity, so that the Ni^{2+} cation can link to both of them.

Thirdly, the optimal value found for the total concentration of adsorption sites corresponds to a surface density of 0.26 OH groups/nm^2, which is lower than the surface OH coverage known for γ-alumina. According to Digne et al. [40], γ-alumina surface exhibits a preferentially exposed (110) surface with a surface OH coverage of approximately 11.8 OH/nm^2 at 573K, whereas the (100) plane of γ-alumina exhibits a surface coverage of 8.8 OH/nm^2 at the same temperature. In the present study, the OH surface coverage should be even higher as impregnation was performed in an aqueous medium and at ambient temperature. These results suggest that not all the OH groups contribute to the adsorption reaction, which indicates a selective affinity of nickel ions for the γ-alumina OH sites depending on their nucleophilic character.

It has commonly been assumed in the literature that alumina surface is characterized by a strong heterogeneity of OH groups, each of them with their own chemical environment and adsorption properties (namely, enthalpy of adsorption) [41]. Upon impregnation with an acidic solution,

surface charge of γ-alumina is slightly positive as a result of protonation of hydroxyl groups. Due to the buffering effect of alumina, the pH of the solution inside the pores tends to rise towards a value of 8, according to the point of zero charge of support. According to the MUSIC model proposed by Hiemstra et al. [42], for a pH approximately equal to 8, negatively charged OH groups ($[(Al_{Oh})OH_2]^{-0.25}$) and neutral ($[(Al_{Oh})_2OH]$) predominate in the (110) surface of γ-alumina, even if some protonated OH groups are still present ($[(Al_{Oh})OH_2]^{+0.5}$) [43,44]. Therefore, the optimal value found for q_t seems to correspond to the quantity of the most reactive OH basic and neutral sites, which are responsible for the formation of covalent bonds with nickel ions [32,45–48]. Note that in Figure 11, model simulations are closer to experimental data for low nickel concentrations (0.05M $[Ni^{2+}]$). Apparently only one type of surface sites contribute to the adsorption reaction in the case of 0.05M $[Ni^{2+}]$, which explains the good agreement between experimental and simulation results. For higher concentrations, the slight discrepancies observed indicate that different types of surface OH sites are involved in the adsorption reaction.

In line with these findings, one can conclude that the optimal value found for K_{ads} rather corresponds to an average value of each K_{ads} characteristic of each OH group. It should be noted that even assuming an average value of K_{ads}, a good agreement between experimental and simulated data was achieved.

Based on the impregnation model, the following description of the phenomena that take place during dry impregnation of nickel based catalysts is proposed. During the contact time between impregnation solution and the support, water travels into the entire porosity of the support thanks to capillary action. Nickel ions in the form of hexa-aqua complexes $[Ni(H_2O)_6]^{2+}$ are not transported together with the capillary flow of water due to a fast adsorption reaction. First, metal ions are adsorbed by exchanging one or more water ligands of the $[Ni(H_2O)_6]^{2+}$ complex with the most reactive surface oxygen atoms of the negatively charged group (AlO^-) leading to inner-sphere surface complexes. Besides, deprotonation reaction of one adjacent neutral hydroxyl group occurs in order to stabilize Ni^{2+} ions through the formation of ion-pairs (Ni^{2+}-O^-Al) [32]. The large value of K_{ads} estimated by the model explains the removal of nickel ions of the fluid phase. Second, nickel ions can be electrostatically adsorbed in the less reactive OH basic sites (having a weaker nucleophilic character). In the diffusive layer, $[Ni(H_2O)_6]^{2+}$ ions diffuse according to their

concentration gradient. One can conclude that impregnation is governed by the available nickel ions that remain in the fluid phase. Thus, for low nickel concentrations, egg-shell profiles are obtained. For more concentrated solutions, more nickel ions are available to diffuse within the support and eventually reach the pellet center.

In case of pre-wetted supports, the main difference in relation to non-wetted supports is the quantity of nickel ions that penetrate into the pellet. For the same nickel concentration in the impregnation solution, the quantity of nickel introduced in the support will be much higher in the case of dry impregnation because part of the metal ions will be transported by capillarity into the pores along with water. For diffusional impregnation, nickel ions penetrate into the pores only by diffusion, which is a much slower process than capillarity, therefore the total quantity of nickel ions deposited in the support is smaller. Therefore, the impregnation method (i.e., the absence or presence of capillarity) directly impacts the diffusion flux and consequently, the final distribution profile: since the quantity of nickel ions that penetrates into the support is higher for non-wetted supports, and knowing that the concentration gradient is the driving force for diffusion, the diffusive flux will be higher for dry impregnation. This results in a thicker final distribution profile for the same nickel concentration in the impregnation solution as illustrated by MRI results in Figure 4 (c) and Figure 6. Besides this difference in the rate of the diffusion flux, the same surface interaction phenomena described for dry impregnation are also valid for diffusional impregnation. Figure 16 shows a schematic picture of the different types of nickel-alumina surface interactions based on the Three Layer Model [49].

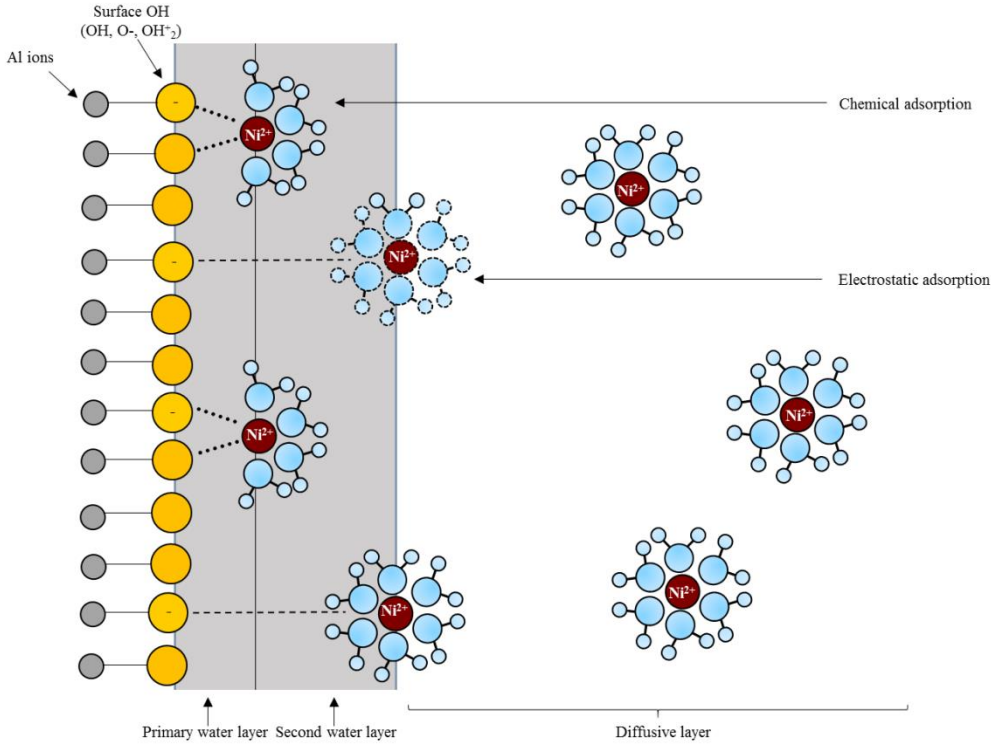

Figure 16 - Schematic picture about phenomena that take place in the interface region during impregnation of γ-alumina with a nickel solution: diffusion in the fluid phase and surface interaction (electrostatic interaction and chemical adsorption) using Three Layer Model (adapted from [4,32,50])

Finally, the parametric sensitivity of the mathematical model shows that the concentration of adsorption groups (q_t) is the key parameter to control the final metal distribution profile. An increase in q_t favors the removal of metal ions from the fluid phase decreasing the available nickel ions to diffusive through the pellet. Therefore, the overall mass transfer decreases and non-uniform nickel profiles are obtained.

5. Conclusion

In this study, a mathematical model to describe impregnation process of Ni/γ-Al_2O_3 catalysts was developed based on in-situ characterization using Magnetic Resonance Imaging. The proposed model couples the phenomena of capillarity, bulk diffusion and adsorption/desorption kinetics. A good agreement between experimental and simulated data was achieved using only two adjustable parameters (total concentration of the active sites of the support and adsorption equilibrium constant). By neglecting the contribution of the Washburn model and using the same optimized

parameters, the same model describes well diffusional impregnation, which illustrates its robustness.

Model predictions showed that the controlling mechanism of the impregnation process is the diffusion of nickel ions in the fluid phase, while the total concentration of the active sites is the key parameter that rules the final nickel distribution profile within the support pellet.

The present model can be applied to improve the impregnation step of the nickel based catalysts, in a way that generates the appropriate active phase profile, which can be either uniform or limited at the outer shell of the support, depending on the catalytic reaction. Also, the model can be used to optimize the support properties (surface and textural properties) according to the desired final metal distribution profile.

Finally, the impregnation model can be extended to more complex impregnation solutions (bimetallic solutions containing or not organic additives) taking into account a competitive adsorption phenomenon and a precise characterization of the nature of the different OH surface sites of alumina. This extended model will be a very useful tool to highlight the key parameters and physicochemical phenomena that control the impregnation process of such complex solutions.

Acknowledgements

The authors wish to thank Dr. D. Sinoquet for her help and advices in the implementation of the optimization procedure.

Declaration of Interests

The authors declare that they have no known competing financial interests or personal relationships that could have appeared to influence the work reported in this paper.

CRediT authorship contribution statement

L. Catita: Conceptualization, Methodology, Investigation, Writing Original Draft, Visualization**. E. Jolimaitre:** Conceptualization, Methodology, Investigation, Writing Original Draft. **A.-A. Quoineaud:** Conceptualization, Writing Reviewing and Editing**. O. Delpoux:** Conceptualization,

Writing Reviewing and Editing. **C. Pichon:** Writing Reviewing and Editing. **J.-M. Schweitzer:** Conceptualization, Methodology, Software, Writing Reviewing and Editing.

References

[1] G. Ert, H. Knozinger, J. Weitkamp, Preparation of Solid Catalysts, Wiley-VCH, Weinheim, Germany, 1999.

[2] A.V. Neimark, L.I. Kheifets, V.B. Fenelonov, Theory of preparation of supported catalysts, Ind. Eng. Chem. Prod. Res. Dev. 20 (1981) 439–450.

[3] E. Marceau, X. Carrier, M. Che, Synthesis of Solid Catalysts, Wiley-VCH, Weinheim, 2009.

[4] K. Bourikas, C. Kordulis, A. Lycourghiotis, The Role of the Liquid-Solid Interface in the Preparation of Supported Catalysts, Catalysis Reviews 48 (2006) 363–444.

[5] J.A. Bergwerff, A.A. Lysova, L. Espinosa-Alonso, I.V. Koptyug, B.M. Weckhuysen, Monitoring transport phenomena of paramagnetic metal-ion complexes inside catalyst bodies with magnetic resonance imaging, Chemistry A European Journal 14 (2008) 2363–2374.

[6] L. Espinosa-Alonso, A.A. Lysova, P. de Peinder, de Jong, Krijn P, I.V. Koptyug, B.M. Weckhuysen, Magnetic resonance imaging studies on catalyst impregnation processes: discriminating metal ion complexes within millimeter-sized gamma-Al_2O_3 catalyst bodies, J. Am. Chem. Soc. 131 (2009) 6525–6534.

[7] A.A. Lysova, J.A. Bergwerff, L. Espinosa-Alonso, B.M. Weckhuysen, I.V. Koptyug, Magnetic resonance imaging as an emerging tool for studying the preparation of supported catalysts, Applied Catalysis A: General 374 (2010) 126–136.

[8] A.A. Lysova, I.V. Koptyug, R.Z. Sagdeev, V.N. Parmon, J.A. Bergwerff, B.M. Weckhuysen, Noninvasive in situ visualization of supported catalyst preparations using multinuclear magnetic resonance imaging, J. Am. Chem. Soc. 127 (2005) 11916–11917.

[9] J.A. Bergwerff, A.A. Lysova, L. Espinosa Alonso, I.V. Koptyug, B.M. Weckhuysen, Probing the transport of paramagnetic complexes inside catalyst bodies in a quantitative manner by magnetic resonance imaging, Angewandte Chemie (International ed. in English) 46 (2007) 7224–7227.

[10] A. Nowacka, J. Moughames, Z. Adem, A.-A. Quoineaud, M. Rolland, F. Guenneau, A. Gédéon, In situ magnetic resonance imaging study of the impregnation of γ-alumina pellets, Applied Catalysis A: General 503 (2015) 111–116.

[11] L. Catita, A.-A. Quoineaud, D. Espinat, C. Pichon, O. Delpoux, Application of Magnetic Resonance Imaging and Raman Imaging to study the impact of phosphorus in impregnation of hydrotreatment catalysts, Applied Catalysis A: General 547 (2017) 164–175.

[12] R. C. Vincent, R. P. Merrill, Concentration profiles in impregnation of porous catalysts, Journal of Catalysis 35 (1974) 206–217.

[13] S. S. Kulkarni, G. R. Mauze, J. A. Schwarz, Concentration profiles and the design of the metal-supported catalysts, Journal of Catalysis 69 (1981) 445–453.

[14] S.-Y. Lee, R. Aris, The Distribution of Active ingredients in Supported Catalysts Prepared by Impregnation, Catalysis Reviews 27 (1985) 207–340.

[15] C. Galarraga, E. Peluso, H. de Lasa, Eggshell catalysts for Fischer-Tropsch synthesis. Modeling catalyst impregnation, Chemical Engineering Journal 82 (2001).

[16] R. Zhang, J.A. Schwarz, Design of inhomogeneous metal distributions within catalyst particles, Applied Catalysis A: General 91 (1992) 57–65.

[17] P. B. Weisz, Sorption-Diffusion in Heterogeneous Systems Part 1 .-General Sorption Behaviour and Criteria, Transactions of the Faraday Society 63 (1967) 1801–1806.

[18] P. B. Weisz, J. S. Hicks, Sorption-Diffusion in Heterogeneous Systems Part 2.-Quantitative Solutions for Uptake Rates, Transactions of the Faraday Society 63 (1967).

[19] P. Harriott, Diffusion effects in the preparation of impregnated catalysts, Journal of Catalysis 14 (1969) 43–48.

[20] O. A. Sceiza, A. A. Castro, D. R. Ardiles, J. M. Parera, Modeling of the Impregnation Step to Prepare Supported Pt/Al_2O_3 Catalysts, Ind. Eng. Chem. Fund. 25 (1986) 84–88.

[21] P. Papageorgiou, D. M. Price, A. Gavriilidis, A. Varma, Preparation of Pt/gamma-Al_2O_3 Pellets with Internal Step-Distribution of Catalyst: Experiments and Theory, Journal of Catalysis 158 (1996) 439–451.

[22] X. Liu, J.G. Khinast, B.J. Glasser, A parametric investigation of impregnation and drying of supported catalysts, Chemical Engineering Science 63 (2008) 4517–4530.

[23] M. Komiyama, R. P. Merrill, H. F. Harnsberger, Concentration Profiles in Impregnation of Porous Catalysts: Nickel on Alumina of Porous Catalysts: Nickel, Journal of Catalysis 63 (1980) 35–52.

[24] E.M. Assaf, L.C. Jesus, J.M. Assaf, The active phase distribution in Ni/Al_2O_3 catalysts and mathematical modeling of the impregnation process, Chemical Engineering Journal 94 (2003) 93–98.

[25] H. Wang, F. Willot, M. Moreaud, M. Rivallan, L. Sorbier, D.Jeulin, Numerical Simulation of Hindered Diffusion in γ -Alumina Catalyst Supports, Oil Gas Sci. Technol. – Rev. IFP Energies nouvelles 72 (2017) 8.

[26] S. Gravina, D. G. Cory, Sensitivity and Resolution of Constant-Time Imaging, Journal of Magnetic Resonance, Series B 104 (1994) 53–61.

[27] J. Hennig, A. Nauerth, H. Friedburg, RARE Imaging: A Fast Imaging Method for Clinical MR, Magn. Reson. Med 3 (1986).

[28] K.C. Metaxas, N.G. Papayannakos, Studying the internal mass transfer phenomena inside a Ni/Al2O3 catalyst for benzene hydrogenation, Chemical Engineering Journal 140 (2008) 352–357.

[29] F. Chauvet, S. Geoffroy, A. Hamoumi, M. Prat, P. Joseph, Roles of gas in capillary filling of nanoslits, Soft Matter 8 (2012) 10738–10749.

[30] V. N. Phan, P. Joseph, L. Djeghlaf, A. E. Dine Allouch, D. Bourrier, P. Abgrall, A.-M. Gué, C. Yang, N.-T. Nguyen, Capillary Filling in Nanochannels—Modeling, Fabrication, and Experiments, Heat Transfer Engineering 32 (2011) 624–635.

[31] Romaric Massard, PhD Thesis - Etude des effets de contraintes sur catalyseurs bimétalliques PdNi supportés, Université Claude Bernard, Lyon, 2006.

[32] L. Vordonis, N. Spanos, P.G. Koutsoukos, A. Lycourghiotis, Mechanism of Adsorption of Co^{2+} and Ni^{2+} Ions on the " Pure and Fluorinated y-Alumina / Electrolyte Solution " Interface (1992) 1736–1743.

[33] Gilbert F. Froment, Kenneth B. Bischoff, Chemical reactor analysis and design, 2nd ed., John Wiley & Sons (Wiley series in chemical engineering), New York, Chichester, Brisbane, 1990.

[34] Robert Byron Bird, Warren E. Stewart, Edwin N. Lightfoot, Transport phenomena, 2nd ed., John Wiley & Sons Inc., New York, Chichester, Brisbane, 2007.

[35] E.W. Washburn, The Dynamics of Capillary Flow, Physical Review 17 (1921) 273–283.

[36] P.-G. de Gennes, F. Brochard-Wyart, D. Quéré, Gouttes, bulles, perles et ondes, Belin, 2002.

[37] J. Buffle, Z. Zhang, K. Startchev, Metal Flux and Dynamic Speciation at (Bio)interfaces. Part I, Environ. Sci. Technol. 41 (2007) 7609–7620.

[38] F.G. Helfferich, Principles of adsorption & adsorption processes, by D. M. Ruthven, John Wiley & sons, 1984, xxiv + 433 pp, AIChe J. 31 (1985) 523–524.

[39] R. Tibshirani, I. Johnstone, T. Hastie, B. Efron, Least angle regression, Ann. Statist. 32 (2004) 407–499.

[40] M. Digne, P. Sautet, P. Raybaud, P. Euzen, H. Toulhoat, Hydroxyl Groups on γ-Alumina Surfaces: A DFT Study, Journal of Catalysis 211 (2002) 1–5.

[41] M. Lagauche, K. Larmier, E. Jolimaitre, K. Barthelet, C. Chizallet, L. Favergeon, M. Pijolat, Thermodynamic Characterization of the Hydroxyl Group on the γ-Alumina Surface by the Energy Distribution Function, J. Phys. Chem. C 121 (2017) 16770–16782.

[42] T. Hiemstra, W. H. Van Riemsdijk, G. H. Bolt, Multisite proton adsorption modeling at the solid/solution interface of (hydr)oxides: a new approach, Journal of colloid and interface science 133 (1989) 91–104.

[43] C. Contescu, J, Jagiello, J. A. Schwarz, Heterogeneity of proton binding sites at the oxide/solution interface, Langmuir 9 (1993) 1754–1765.

[44] C. Contescu, J. HuS, J. A. Schwarz, 1 -pK Multisites Description of Charge Development Alumina Interface, J. Chem. Faraday Trans. 89 (1993) 4091–4099.

[45] F. Négrier, E. Marceau, M. Che, J.-M. Giraudon, L. Gengembre, A. Löfberg, A systematic study of the interactions between chemical partners (metal, ligands, counterions, and support) involved in the design of Al_2O_3-supported nickel catalysts from diamine-Ni(II) chelates, Journal of Physical Chemistry. B 109 (2005) 2836–2845.

[46] N. Spanos, A. Lycourghiotis, Mechanism of deposition of Co^{2+} and Ni^{2+} ions on the interface between pure and F^- - doped γ-alumina and the impregnating solution, Journal of the Chemical Society, Faraday Transactions 89 (1993) 4101.

[47] C. J. Chisholm-Brause, P. A. O'Day, G. E. Brown Jr, G. A. Parks, Evidence for multinuclear metal-ion complexes at solid-water interfaces from X-ray absorption spectroscopy, Nature 348 (1990) 528–531.

[48] J. Vakros, K. Bourikas, S. Perlepes, C. Kordulis, A. Lycourghiotis, Adsorption of cobalt ions on the "electrolytic solution/gamma-alumina" interface studied by diffuse reflectance

spectroscopy (DRS), Langmuir the ACS journal of surfaces and colloids 20 (2004) 10542–10550.

[49] K. Bourikas, C. Kordulis, J. Vakros, A. Lycourghiotis, Adsorption of cobalt species on the interface, which is developed between aqueous solution and metal oxides used for the preparation of supported catalysts: a critical review, Advances in colloid and interface science 110 (2004) 97–120.

[50] J. Moreau, PhD Thesis - Rationalisation of the impregnation step of catalysts on the basis of molybdenum heteropolyanions supported on alumina, Université Claude Bernard, Lyon, 2012.

[51] N. Midoux, Mécanique et Rhéologie des fluides en génie chimique, Technique et Documentation - Lavoisier, 1985.

Supplementary Data

Appendix A

Upon dry impregnation, replacement of fluid inside the pore space (called capillary) by impregnation solution takes place through the action of capillary forces. Figure A. 1 shows a schematic picture of a cylindrical pore with radius R_{pore} in contact with the impregnation solution.

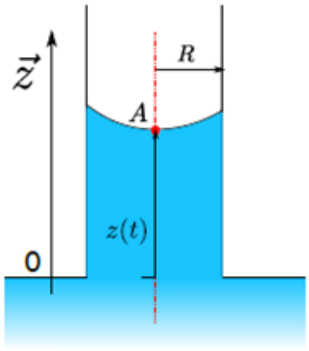

Figure A. 1 - Capillary in contact with wetting fluid

The evolution of the distance travelled by the liquid into the pore (z) as a function of time (t) depends on three different forces: capillary force, $\vec{F}_{capillary}$, friction force , $\vec{F}_{friction}$ and gravity force, $\vec{P}$, which is negligible compared to the first ones [1].

The formation of bubbles that can occur in closed end pores was neglected (the gas phase is supposed to evacuate instantly from the pores).

The following paragraphs explain how to obtain z(t) based on Washburn model.

The linear momentum balance with respect to a control volume is given by the following equation [1]:

$$\begin{aligned}&(Sum\ of\ forces\ acting\ on\ control\ volume)\\&=(Rate\ of\ momentum\ out\ of\ control\ volume)\\&-(Rate\ of\ momentum\ into\ control\ volume)\\&+(Rate\ of accumulation\ of\ momentum\ within\ control\ volume)\end{aligned}$$ **Eq. A. 1**

Recalling the conservation of linear moment and Newton's second law, Eq. A. 1 results in:

$$\sum \vec{F} = \frac{d(m.\vec{v})}{dt}$$ **Eq. A. 2**

Where,

$\Sigma\vec{F}$ is the sum of forces acting on control volume,

m corresponds to mass,

$\overrightarrow{v}$ corresponds to velocity

t stands for time.

The evolution of the solution front is a result of capillary and friction forces Eq. A. 2 can be written as:

$$\frac{d(m.\vec{v})}{dt} = \vec{F}_{capillary} + \vec{F}_{friction} \qquad \textbf{Eq. A. 3}$$

Capillary force applied in the cross section (S) of the cylindrical pore is based on Young-Laplace equation ($\Delta P_{Laplace}$) and is defined in Eq. A. 4.

$$F_{capillary} = \Delta P_{Laplace} \cdot S = \frac{2 \cdot \gamma \cdot cos\theta}{R_{pore}} \cdot \pi \cdot R_{pore}^2 \leftrightarrow \qquad \textbf{Eq. A. 4}$$

$$F_{capillary} = 2 \cdot \pi \cdot R_{pore} \cdot \gamma \cdot cos\theta \qquad \textbf{Eq. A. 5}$$

Where,

R_{pore} stands for the pore radius,

γ is the interfacial tension,

θ is the wetting angle of the wetting fluid on the surface of the capillary.

To define the **friction force**, a linear momentum balance within the control volume schematized in Figure A. 2, which represents the section of a cylindrical tube of radius R and length L is required. The following assumptions are adopted [51]:

- Incompressible, continuous, Newtonian and viscous fluid flowing at steady state within a cylindrical tube
- Fully developed fluid, which means that velocity profile does not change along the flow direction (in this case, z)

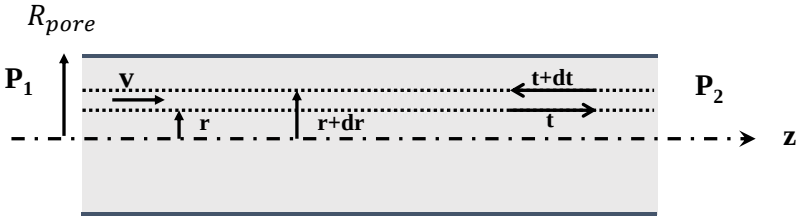

Figure A. 2 - Control volume for a flow within a cylindrical tube of radius R [51]

The momentum balance equation is based on Eq. A. 1. Since the velocity profile does not change along z direction, the resulting force acting on the system is zero. This resulting force is composed of:

- Viscous friction forces (related with shear stress tensor τ), due to radial motion of momentum at a molecular scale
- Pressure forces (P) exerted at the extremities
- Gravity force, which is negligible compared to the first ones [51]

Additionally, the accumulation term is also zero.

Therefore, the linear momentum balance with respect to the control volume schematized in Figure A. 2 is given in Eq. A. 6.

$$(P_1 - P_2) \cdot 2 \cdot \pi \cdot r \cdot dr + 2 \cdot \pi \cdot r \cdot z \cdot \tau - 2 \cdot \pi \cdot (r + dr) \cdot z \cdot (\tau + d\tau) = 0 \qquad \textbf{Eq. A. 6}$$

With,

$$\tau + d\tau = \tau + \frac{d\tau}{dr} dr \qquad \textbf{Eq. A. 7}$$

Rearranging Eq. A. 6 the following relation (Eq. A. 8) is obtained, where $\Delta P_{friction} = P_1 - P_2$:

$$d(r \cdot \tau) = \frac{\Delta P_{friction} \cdot r \cdot dr}{L} \qquad \textbf{Eq. A. 8}$$

Where,

$$\tau = \frac{\Delta P_{friction} \cdot r}{2L} + \frac{Cte}{r} \qquad \textbf{Eq. A. 9}$$

The first boundary condition is given by:

$$r = 0 : \tau \neq \infty$$

Thus, shear stress is defined in the following equation.

$$\tau = \frac{\Delta P_{friction} \cdot r}{2L} \qquad \textbf{Eq. A. 10}$$

This relation is valid for all viscous fluids in laminar flow in a cylindrical tube. As one of the hypothesis stated is that the fluid is a Newtonian one, the shear stress is given by:

$$\tau = -\mu \cdot \frac{dv}{dr} \qquad \textbf{Eq. A. 11}$$

Where,

μ is the shear viscosity of the fluid

dv/dr is the velocity gradient that corresponds to the deformation rate of a fluid element.

Combining Eq. A. 10 and Eq. A. 11 and integrating between radius, r and pore radius, R_{pore}:

$$\int_{v_r}^{v_{wall}} dv = \int_{r}^{R_{pore}} -\frac{\Delta P_{friction} \cdot r \cdot dr}{2 \cdot \mu \cdot z} \quad \textbf{Eq. A. 12}$$

To solve integral given by Eq. A. 12, a second boundary condition is necessary.

$$r = R_{pore}: v = 0$$

Therefore, Eq. A. 12 gives:

$$v(r) = \frac{\Delta P_{friction}}{4 \cdot \mu \cdot z} \cdot \left(r^2 - R_{pore}^2\right) \quad \textbf{Eq. A. 13}$$

The average velocity is given by:

$$\bar{v} = \frac{\int_0^{2\pi} \int_0^R v\,(r).rdrd\theta}{\pi R^2} \quad \textbf{Eq. A. 14}$$

Hence, the average velocity results in Eq. A. 14, which corresponds to Hagen-Poiseuille equation that relates the average flow velocity with the pressure drop due to friction.

$$\bar{v} = \frac{\Delta P_{friction} \cdot R_{pore}^2}{8 \cdot \mu \cdot z} \quad \textbf{Eq. A. 15}$$

Finally, friction force ($F_{friction}$) applied in the cross section (S) of the cylindrical pore is defined in Eq. A. 16:

$$F_{friction} = \Delta P_{friction} \cdot S \Leftrightarrow \\ F_{friction} = 8 \cdot \pi \cdot \mu \cdot z.\bar{v} \quad \textbf{Eq. A. 16}$$

The friction force is more important as velocity increases. It is also proportional to the length z of the tube. Eq. A. 17 is then used to calculate the capillary impregnation dynamics, in which $\bar{v}$ represents the penetration rate, which is given by the following equation:

$$\bar{v} = \frac{dz}{dt} \quad \textbf{Eq. A. 17}$$

Washburn model [2] is used to calculate the penetration rate. This model is valid for low Reynolds number ($Re < 1$) and viscous fluid. It is also assumed that the flow of the impregnation solution in the pore is characterized by Poiseuille steady stated. Therefore, the small inertia effects are neglected. According to Washburn model, becomes:

$$\frac{d(m.\vec{v})}{dt} = \vec{F}_{capillary} + \vec{F}_{friction} = 0 \quad \textbf{Eq. A. 18}$$

Combining Eq. A. 5, Eq. A. 16 and Eq. A. 18, one obtains:

$$2 \cdot \pi \cdot R_{pore} \cdot \gamma \cdot cos\theta - 8 \cdot \pi \cdot \mu \cdot z.\bar{v} = 0 \quad \textbf{Eq. A. 19}$$

Combining Eq. A. 17 and Eq. A. 19, it results:

$$\frac{dz^2}{dt} = \frac{R_{pore} \cdot \gamma \cdot cos\theta}{2 \cdot \mu} \qquad \textbf{Eq. A. 20}$$

Assuming that $z(0) = 0$, the **distance z that the impregnation solution travels into the pore** is given by:

$$z = \sqrt{\frac{R_{pore} \cdot \gamma \cdot cos\theta}{2 \cdot \mu} \cdot t} \qquad \textbf{Eq. A. 21}$$

[1] N. Midoux, Mécanique et rhéologie des fluides en génie chimique, Tec & Doc, 1993.

[2] E.W. Washburn, The Dynamics of Capillary Flow, Physical Review 17 (1921) 273–283

Appendix B

In order to validate the metal distribution profiles observed by ^{1}H MRI, the same impregnated samples were characterized by EPMA technique. To this end, the radial intensity profiles of MRI images and the average metal concentration profiles obtained by EPMA were compared. The radial intensity profiles as a function of the distance from the edge of the support were obtained through image processing as described in [3]. These profiles were then corrected by a constant factor in order to take into account the relaxation times dependence as well as by a scaling factor applied by the MRI software in each image, as described in the following paragraphs.

First, the software ImageJ is used to export MRI image data into 16bit.tiff files. From these data, an IFPEN software for image processing [4] is used to calculate on each image the radial intensity profiles as a function of the distance from the edge of the support. For each distance, a minimum, a maximum and an average intensity are computed, and provide associated profiles. In this study, the measured intensity profiles are referred as the apparent intensity (I) profiles as they do not take into account neither relaxation times dependence nor normalization carried out by Paravision software.

These apparent intensity profiles (I) are corrected with K factor (see Eq. B. 1 [5]) in order to take into account the relaxation times dependence.

$$\mathrm{I} = \mathrm{I}_0 \, K \qquad \textbf{Eq. B. 1}$$

In Eq. B. 1, I_0 is the signal that would be measured immediately following a 90° pulse and K is defined according to Eq. B. 2:

$$K = e^{-t_p/T_2^*} G\left(\frac{TR}{T_1}, \alpha\right) \quad \textbf{Eq. B. 2}$$

Where t_p corresponds to the encoding time, T_2^* corresponds to the transverse relaxation and $G(TR/T_1, \alpha)$ describes the signal attenuation from the Ernst-angle excitation pulse, α (see Eq. B. 3).

$$G = \frac{1 - E}{1 - E^2} \sin(\alpha) \quad \textbf{Eq. B. 3}$$

Where,

$$\cos(\alpha) = E = e^{-TR/T_1} \quad \textbf{Eq. B. 4}$$

In Eq. B. 4, TR corresponds to the repetition time and T_1 corresponds to the longitudinal relaxation.

Additionally, the apparent intensity profiles (I) are also corrected by the scaling factor of each image applied by Paravision software (Visu Core Data Slope parameter). The mathematical equation to obtain average radial intensity profiles (I_0) is shown in Eq. B. 5.

$$I_0 = \frac{I \times Scaling\ factor}{K} \quad \textbf{Eq. B. 5}$$

The comparison between average concentration profiles obtained by EPMA and the corrected radial intensity profiles (I_0) obtained by MRI is shown in Figure B. 1. The shaded area delimits the maximum and minimum radial intensity profiles. Both techniques show the presence of nickel ions in the same positions of the catalyst pellet regarding the spatial resolution of each technique. Slight differences may be observed due to the signal to noise ratio of MRI images, since the sensitivity of MRI technique is lower than EPMA. Yet, no quantitative information about the evolution of the concentration profile of nickel ions inside the pellet can be obtained through this approach.

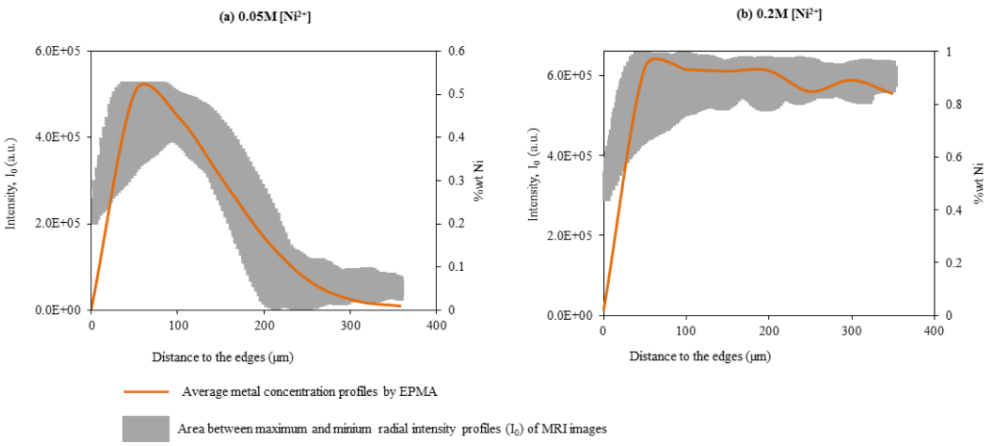

Figure B. 1 - Comparison between average metal concentration profiles by EPMA (spatial resolution of 50 µm) and radial intensity profiles I_0 obtained through image processing of MRI images (spatial resolution resulting from image processing is increased to 14µm/pixel by means of high quality spline interpolation [6]). Both analyses were carried out in the same γ-alumina pellet at equilibrium state after dry impregnation corresponding to approximately (a) 12h in the case of with 0.05M [Ni^{2+}] solution and (b) 30 min in the case of 0.2M [Ni^{2+}] solution. Shaded area delimits the maximum and minimum radial intensity profiles (I_0).

[3] L. Catita, A.-A. Quoineaud, D. Espinat, C. Pichon, O. Delpoux, Impact of Citric Acid on the Impregnation of CoMoP/γ-Al2O3 Catalysts: Time and Spatially Resolved MRI and Raman Imaging Study, Topics in Catalysis (2018) 1474–1484.

[4] M. Moreaud, F. Cokelaer, Flowing Bilateral Filter: Definition and Implementations, Image Anal Stereol 34 (2015) 101–110.

[5] S. Gravina, D.G. Cory, Sensitivity and Resolution of Constant-Time Imaging, Journal of Magnetic Resonance, Series B 104 (1994) 53–61.

[6] P. Thévenaz, T. Blu, M. Unser, Interpolation revisited, IEEE Transactions on Medical Imaging 19 (2000) 739–758.

Appendix C

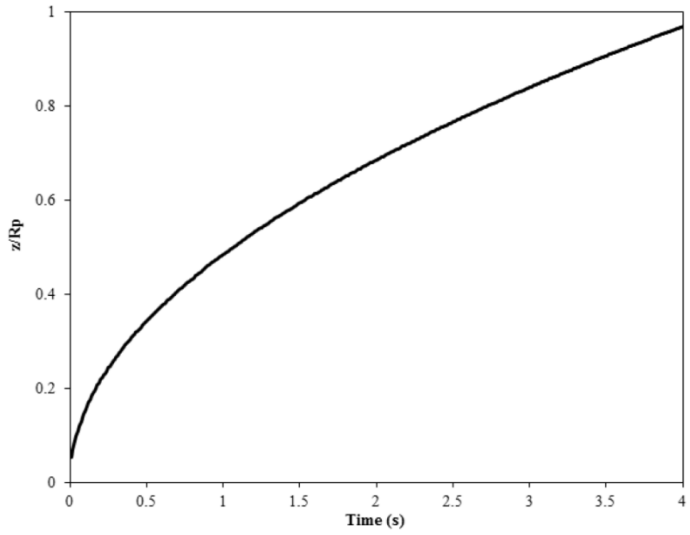

Figure C. 1 - Evolution of advancing front of water calculated from (Eq. **4**) as a function of time: z corresponds to the distance travelled by liquid into the pore (m) and R_p to the porous radius (m)

Appendix D

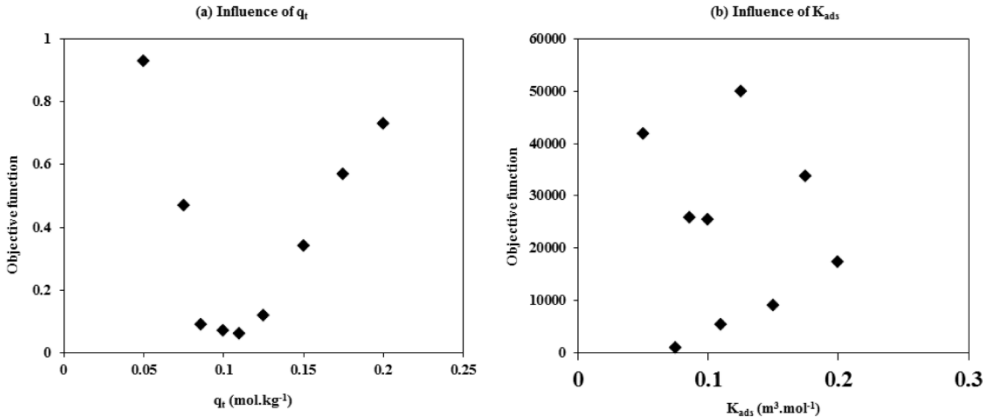

Figure D.1 - Influence of the parameters (a) $\boldsymbol{q_t}$ and (b) $\boldsymbol{K_{ads}}$ on the objective function (see (Eq. **8**)

Tables

Table 1 – Characteristic parameters for simulation of impregnation profiles

Table 2 – Design plan of simulation and optimization results

Table 3 – Model parameters

Figure Captions

Figure 1 – Protocol of "dry" impregnation using a non-wetted support (closest of the traditional incipient wetness impregnation)

Figure 2 – Protocol of "diffusional" impregnation using a pre-wetted support

Figure 3 – Physicochemical phenomena involved in the impregnation (capillarity only for dry impregnation) (adapted from [3])

Figure 4 – ^{1}H MRI images recorded on γ-alumina pellets at several points in time after dry impregnation with (a) 0.05M [Ni^{2+}] (b) 0.08M [Ni^{2+}] solutions (c) 0.1M [Ni^{2+}] solutions and (d) 0.2M [Ni^{2+}] solutions. These images correspond to the center of the pellet.

Figure 5 - ^{1}H MRI images corresponding to transport of 0.05 M [Ni^{2+}] solutions within the porosity of a γ-Al_2O_3 pellet at different positions along the z axis (z=0 corresponds to the pellet center) after 11 minutes of dry impregnation (L corresponds to the pellet length)

Figure 6 - ^{1}H MRI images recorded on γ-alumina pellet at several points in time after diffusional impregnation with 0.1M [Ni^{2+}] solution. These images correspond to the center of the pellet.

Figure 7 - Model simulations for nickel concentration profiles after 11h of dry impregnation using 0.05M [Ni^{2+}] solution: evolution of nickel concentration profiles in the (a) adsorbed and (b) fluid phase as a function of the pellet radius with and without surface diffusion (q_t, K_{ads})=(0.11, 5500)

Figure 8 - Model simulations for nickel concentration profiles after 11h of dry impregnation using 0.05M [Ni^{2+}] solution: evolution of nickel concentration profiles in the (a) adsorbed and (b) fluid phase as a function of the pellet radius with and without surface diffusion ($\boldsymbol{q_t}$, $\boldsymbol{K_{ads}}$)=(0.05, 41833)

Figure 9 – Model predictions for nickel distribution profiles at several points in time after dry impregnation for various nickel concentrations

Figure 10 - Model predictions for nickel distribution profiles at several points in time after diffusional impregnation for 0.1M [Ni^{2+}]

Figure 11 – Comparison between experimental and simulated data (using $(\boldsymbol{q_t}, \boldsymbol{K_{ads}})$ = (0.11, 5500) in case of (a) dry impregnation for different nickel concentrations: 0.05M [Ni^{2+}] (in grey), 0.08M [Ni^{2+}] (in green), 0.1M [Ni^{2+}] (in orange), 0.2M [Ni^{2+}] (in blue) and (b) diffusional impregnation with 0.1M [Ni^{2+}] (in purple)

Figure 12 – ^{1}H MRI images at the center of the pellet (top) and model simulations (bottom) recorded on γ-Al_2O_3 pellet at several points in time after dry impregnation with 0.07M [Ni^{2+}] solution.

Figure 13 - ^{1}H MRI images at the center of the pellet (top) and model simulations (bottom) recorded on γ-Al_2O_3 pellet at several points in time after diffusional impregnation with 0.2M [Ni^{2+}] solution.

Figure 14 – Simulations of nickel distribution profiles for dry impregnation with 0.05M [Ni] obtained by varying the optimal $\boldsymbol{q_t}$ (represented in grey) in $\pm$ 10% (represented in orange : solid line corresponds to -10% and the dashed line to +10%) and in $\pm$ 50% (represented in blue: solid line corresponds to -50% and the dashed line to +50%). The points in grey correspond to the experimental data. For these simulations $\boldsymbol{K_{ads}}$ = 5500 $m^3.mol^{-1}$.

Figure 15 - Simulations of nickel distribution profiles for dry impregnation with 0.05M [Ni] obtained by varying the optimal $\boldsymbol{K_{ads}}$ (represented in grey) in $\pm$ 50% (represented in blue: solid line corresponds to -50% and the dashed line to +50%). Simulations for irreversible adsorption (in purple) and neglecting adsorption (in green) are also shown. The points correspond to the experimental data. For these simulations $\boldsymbol{q_t}$ = 0.11 $mol.kg^{-1}$. Simulations by varying the $\boldsymbol{K_{ads}}$ in $\pm$ 10% are not shown here: no influence of observed in this range of variation.

Figure 16 - Schematic picture about phenomena that take place in the interface region during impregnation of γ-alumina with nickel solution: diffusion in the fluid phase and surface interaction (electrostatic interaction and chemical adsorption) using Three Layer Model (adapted from [4,32,50])